

Non-universal transport mechanisms in vertical natural convection with dispersed light droplets

Chong Shen Ng^{1,†}, Vamsi Spandan², Roberto Verzicco^{1,3,4} and Detlef Lohse^{1,5,‡}

¹Physics of Fluids Group, Max Planck Center for Complex Fluid Dynamics, J. M. Burgers Center for Fluid Dynamics and MESA+ Research Institute, Department of Science and Technology, University of Twente, 7500AE Enschede, The Netherlands

²School of Engineering and Applied Sciences, Harvard University, Cambridge, MA 02138, USA

³Gran Sasso Science Institute - Viale F. Crispi, 7 67100 L'Aquila, Italy

⁴Dipartimento di Ingegneria Industriale, University of Rome 'Tor Vergata', Roma 00133, Italy

⁵Max Planck Institute for Dynamics and Self-Organisation, 37077 Göttingen, Germany

(Received xx; revised xx; accepted xx)

We present results on the effect of dispersed droplets in vertical natural convection (VC) using direct numerical simulations based on a two-way fully coupled Euler–Lagrange approach with a liquid phase and a dispersed droplets phase. For increasing thermal driving, characterised by the Rayleigh number, Ra , of the two analysed droplet volume fractions, $\alpha = 5 \times 10^{-3}$ and $\alpha = 2 \times 10^{-2}$, we find non-monotonic responses to the overall heat fluxes, characterised by the Nusselt number, Nu . The Nu number is larger when the droplets are thermally coupled to the liquid. However, Nu retains the effective scaling exponents that are close to the 1/4-laminar VC scaling, suggesting that the heat transport is still modulated by thermal boundary layers. Local analyses reveal the non-monotonic trends of local heat fluxes and wall-shear stresses: Whilst regions of high heat fluxes are correlated to increased wall-shear stresses, the spatio-temporal distribution and magnitude of the increase is non-universal, implying that the overall heat transport is obscured by competing mechanisms. Most crucially, we find that the transport mechanisms inherently depend on the dominance of droplet driving to thermal driving that can be quantified by (i) the bubble parameter b , which measures the ratio of energy produced by the dispersed phase and the energy of the background turbulence, and (ii) Ra_d/Ra , where Ra_d is the droplet Rayleigh number, which we introduce in this paper. When $b \lesssim O(10^{-1})$ and $Ra_d/Ra \lesssim O(100)$, the Nu scaling is expected to recover to the VC scaling without droplets, and comparison with b and Ra_d/Ra from our data supports this notion.

1. Introduction

Bubbles are ubiquitous. Within a liquid, they can play an important role in the transport of mass and heat. Such complex interactions of bubbles and liquids can be found in various applications and process technologies, for example in cooling systems of power plants, metallurgical industries, catalytic reactions and in the mixing of chemicals (Brennen 2005; Balachandar & Eaton 2010; Mathai *et al.* 2020). One commonly studied class of bubble-liquid interaction is the bubble column (Mudde 2005), where liquid

† Email address for correspondence: c.s.ng@utwente.nl and
‡ d.lohse@utwente.nl

turbulence is generated and sustained by a rising swarm of bubbles. This form of turbulence is typically referred to as pseudo-turbulence (Lance & Bataille 1991; van Wijngaarden 1998; Mercado *et al.* 2010) or bubble-induced agitation (Risso 2018).

Various parameters can be controlled to modulate heat transport in a bubbly flow. For instance, one can use microbubbles to increase heat transport in the boundary layer (Kitagawa & Murai 2013) or by inclining the domain (Piedra *et al.* 2015). The fluid properties can also be varied. For example, Deen & Kuipers (2013) studied the effects of bubble deformability and found localised increase of heat fluxes when bubble coalescence prevails in the near-wall region, whereas Dabiri & Tryggvason (2015) showed that nearly spherical bubbles tend to aggregate at the walls, which in turn agitate the thermal boundary layers and result in higher heat transport than for the case with deformable bubbles. From these studies, one key observation that can be made is that heat transport enhancement has been largely linked to boundary layer effects, e.g. thinning of the thermal boundary layers or ejection of thermal plumes. On the other hand, a recent experimental campaign using a homogeneous bubble column found that the heat transport, characterised by the Nusselt number Nu , not only increases by up to 20 times, but also becomes insensitive to the thermal driving of the background flow, characterised by the Rayleigh number Ra (Gvozdić *et al.* 2018, 2019). The Ra -insensitivity persists across a range of bubble volume fractions α between 5×10^{-3} and 5×10^{-2} , implying that bubble-induced liquid agitation overwhelmingly dominates the heat transport mechanism across the thermal boundary layers. Indeed, the multifold enhancement in Nu is consistent with engineering estimates in the design of bubble column gas-liquid reactors (Deckwer 1980).

Is there, however, any link between bubbly flows that directly influence the boundary layers versus bubble column experiments? And if any, are the boundary layers affected by the dispersed phase in a universal manner when $\alpha > 0$? In this paper, we ask the question of how other parameters, specifically the density ratio of the dispersed phase to liquid phase, influence heat transport. Inspired by the water column experiments in Gvozdić *et al.* (2018) and to make contact with recent studies, we selected a setup of natural convection in a rectangular cell containing a dispersed phase consisting of freely rising and deformable light droplets.

The model setup of the flow is thermal natural convection, in particular, a flow sustained by applying a temperature difference between two opposing walls. Classical examples of thermal natural convection include Rayleigh–Bénard convection (Ahlers *et al.* 2009), where the hot wall is at the bottom and the cold wall at the top, and horizontal convection (Hughes & Griffiths 2008; Shishkina *et al.* 2016), where heating and cooling is applied at the same horizontal level. When the flow is confined between a hot vertical wall and a cold vertical wall, gravity acts orthogonal to the heat flux and this setup is referred to as vertical natural convection (VC). For confined VC, the bulk flow is quiescent (see mean profiles in figure 1*a* and visualisation in 1*b*) and at low Ra , the laminar-like boundary layers are expected to dominate heat and momentum transport (Shishkina 2016). This flow is unlike the unconfined, doubly-periodic VC (Ng *et al.* 2015, 2017) where a mean shear is present and determines heat transport in the bulk flow region (Ng *et al.* 2018). Hereinafter, we refer to the rectangular VC cell setup as VC, for simplicity.

When light droplets are introduced into VC, we ask two specific questions:

- Are the heat and momentum transport statistics universal for droplets (i.e. when the density of droplets are close to the density of the liquid)?
- How important is the role of thermal coupling between the droplets and the liquid?

To answer these questions, we perform direct numerical simulations (DNS) of VC

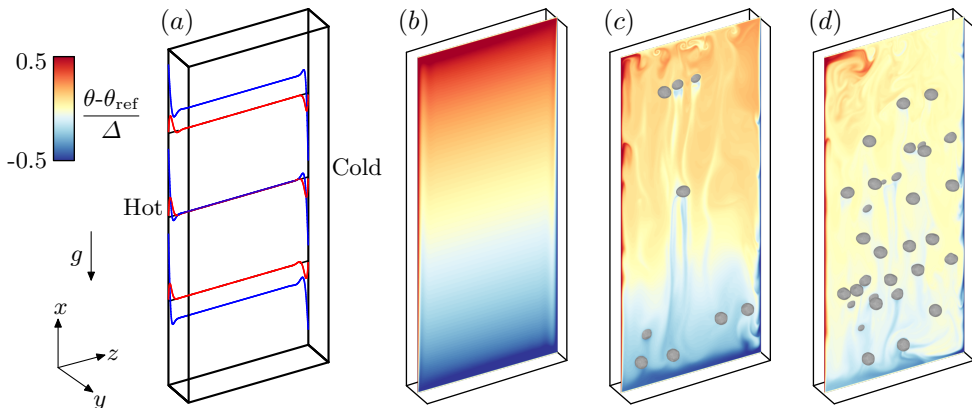


FIGURE 1. Visualisations of instantaneous temperature fields for VC at Rayleigh number of 2×10^8 . In (a), the red and blue curves correspond to mean velocity and temperature profiles at $x = 0.25L_x$, $0.5L_x$ and $0.75L_x$, respectively, at $\alpha = 0$. Volume fractions shown are (b) $\alpha = 0$, (c) 5×10^{-3} , and (d) 2×10^{-2} . Rendered flow fields are for droplets with mechanical coupling.

with droplets where we have control over the density ratio and thermal coupling of the droplet phase to the liquid phase. The droplets are fully coupled to the liquid phase DNS using the immersed boundary method (IBM) and the interaction potential approach, both of which are versatile numerical methodologies to simulate fully-coupled fluid flows with deformable interfaces (e.g. Spandan *et al.* 2018b; Meschini *et al.* 2018; Viola *et al.* 2020). Furthermore, IBM offers some computational advantages over existing numerical methods for multiphase flows (e.g. volume-of-fluid, level-set and front tracking), for instance, the underlying discretised grid is fixed and no sharp interfaces need to be resolved (Spandan *et al.* 2017). Recent advancements in the numerical methodology have allowed the use of sparser discretisations of the deformable interface relative to the underlying grid (Spandan *et al.* 2018a) without compromising numerical accuracy, further easing the computational requirements for large-scale multiphase flows. The disadvantage of IBM, however, is that droplet coalescence or splitting is hard to model and correspondingly in this paper we refrain from attempting to do so.

Our paper is organised as follows: in §2, we first describe the flow setup and numerical details for the fluid and dispersed phase. In §3, the numerical results are examined in detail. By analyzing the near-wall heat fluxes (§4) and wall-shear stresses (§5), we relate the droplet driving dynamics to changes in the near-wall statistics. In §6, we discuss and compare the influence of our selected parameters and the experimental parameters as reported in Gvozdić *et al.* (2018). Finally, in §7, we summarise our results and provide an outlook.

2. Flow setup

Our reference setup is the single-phase VC flow (figure 1b), which is a buoyancy driven flow confined between two differentially heated vertical walls and two adiabatic horizontal walls. This reference flow will be referred to as the liquid carrier phase. The flow is governed by mass conservation, balances of momentum and energy conservation which

within the Boussinesq approximation read,

$$\partial_i u_i = 0, \quad (2.1)$$

$$\partial_t u_i + u_j \partial_j u_i = -\frac{1}{\rho_{\text{ref}}} \partial_i p + \delta_{i1} g \beta (\theta - \theta_{\text{ref}}) + \nu \partial_j^2 u_i + f_i, \quad (2.2)$$

$$\partial_t \theta + u_j \partial_j \theta = \kappa \partial_j^2 \theta + q_i, \quad (2.3)$$

where $\partial_t \equiv \partial/\partial t$, $\partial_i \equiv \partial/\partial x_i$, ($i, j = 1, 2, 3$) and repeated indices imply summation. In (2.2), f_i is the back-reaction forces of the dispersed phase on the fluid and for single-phase VC, $f_i = 0$. The thermal analogue to f_i in (2.2) is q_i in (2.3), which we selectively enable or disable in the present study. We define ρ_{ref} as the reference density, θ_{ref} as the reference temperature, and β is the thermal expansion coefficient of the fluid, ν the kinematic viscosity and κ the thermal diffusivity, all assumed to be independent of temperature. The unit length is defined as the distance between the heated plates, L_z , and the streamwise and spanwise domain lengths are $L_x = 2.4L_z$ and $L_y = 0.25L_z$, respectively. Hereinafter, all lengthscales are non-dimensionalized by L_z . No-slip and no-penetration boundary conditions are imposed on the velocity at all four walls, whereas periodic boundary conditions are imposed in the y -direction. The left and right walls are imposed with temperatures hotter and cooler than the reference temperature $\theta_{\text{ref}} \equiv (\theta_h + \theta_c)/2$. The control parameters are the Rayleigh and Prandtl numbers, which are respectively defined as

$$Ra \equiv \frac{g\beta\Delta L_z^3}{\nu\kappa}, \quad Pr \equiv \frac{\nu}{\kappa}, \quad (2.4a,b)$$

where $\Delta \equiv \theta_h - \theta_c$. The aspect ratio can also be an additional control parameter for confined thermal convection problems (van der Poel *et al.* 2011; Zwirner & Shishkina 2018), but at present, we restrict our analyses to a fixed value. Our simulations cover the values of $Ra = 1.3 \times 10^8$ - 1.3×10^9 and for $Pr = 7$, corresponding to water.

The typical flow response is described by the Nusselt and Reynolds numbers,

$$Nu \equiv \frac{f_w L_z}{\Delta \kappa}, \quad Re \equiv \frac{U_s L_z}{\nu}, \quad (2.5a,b)$$

which quantify the dimensionless heat flux and degree of turbulence, respectively. In (2.5a), $f_w \equiv -\kappa(d\bar{\theta}/dz)|_w$ is the wall heat flux and $(\cdot)|_w$ denotes the wall value. U_s is the ‘wind’-based velocity scale for VC (Ng *et al.* 2015) and accordingly, we set $U_s \equiv \bar{u}_{\text{max}}$, which is the maximum mean vertical velocity. The notation (\cdot) denotes time and xy -averaged quantities, and the notation $(\cdot)'$ denotes the fluctuating component, e.g. $u' = u - \bar{u}$. With the addition of the thermal forcing term, q_i , in (2.3), a different definition for Nu becomes necessary because $(d\bar{\theta}/dz)|_{z=0} \neq (d\bar{\theta}/dz)|_{z=L_z}$ and the mean temperature equation now obeys $w'\theta'(z) - \kappa\partial_z\bar{\theta} - \bar{q}_i = \text{const.}$. To overcome this difficulty, we employ the dissipation rate-based definition for the Nusselt number:

$$Nu \equiv \frac{\varepsilon_\theta}{\kappa(\Delta/L_z)^2} = \frac{\langle \theta_h (d\bar{\theta}/dz)_h - \theta_c (d\bar{\theta}/dz)_c \rangle}{\Delta^2/L_z} + \frac{\langle \theta \cdot q_i \rangle}{\kappa(\Delta/L_z)^2}, \quad (2.6)$$

where ε_θ is the volume-averaged thermal dissipation due to turbulent fluctuations and $\langle \cdot \rangle$ denotes time- and volume-averaged quantities. When $q_i = 0$, (2.6) equals to (2.5a). The definition in (2.6) is also a direct analogue to the drag reduction calculations for multiphase Taylor–Couette flows (e.g. Sugiyama *et al.* 2008; Spandan *et al.* 2018b), making it convenient when comparing heat transport at matched Ra (discussed in §3.5). Throughout this paper, we will use (2.6) when reporting values of Nu , unless defined otherwise.

	Ra ($\times 10^9$)	α ($\times 10^{-2}$)	Δx^+	Δy^+	Δz_w^+	Δz_c^+	$T_s/(L_z/U_\Delta)$	$T_s/\langle t_d \rangle$
	0.1	-	0.8	0.8	0.3	1.1	400	-
	0.2	-	1.0	1.0	0.3	1.4	570	-
	0.4	-	1.3	1.3	0.4	1.7	570	-
	0.7	-	1.3	1.3	0.3	1.8	480	-
	1.3	-	1.6	1.6	0.4	2.2	470	-
Mech. coupling	0.1	0.5	0.9	0.9	0.3	1.2	250	44
	0.2	0.5	1.1	1.1	0.3	1.5	190	24
	0.4	0.5	1.4	1.3	0.4	1.9	230	22
	0.7	0.5	1.3	1.3	0.4	1.9	320	22
	1.3	0.5	1.6	1.6	0.4	2.3	400	21
	0.1	2.0	0.9	0.9	0.3	1.3	230	40
	0.2	2.0	1.1	1.1	0.3	1.5	220	27
	0.4	2.0	1.4	1.3	0.4	1.9	240	22
	0.7	2.0	1.4	1.4	0.4	1.9	300	21
	1.3	2.0	1.7	1.7	0.5	2.4	390	21
Mech.+therm. coupling	0.1	0.5	0.9	0.9	0.3	1.2	220	39
	0.2	0.5	1.1	1.1	0.3	1.5	210	27
	0.4	0.5	1.4	1.3	0.4	1.9	260	25
	0.7	0.5	1.3	1.3	0.4	1.9	320	22
	1.3	0.5	1.6	1.6	0.4	2.3	410	22
	0.1	2.0	0.9	0.9	0.3	1.3	200	36
	0.2	2.0	1.1	1.1	0.3	1.5	200	26
	0.4	2.0	1.4	1.3	0.4	1.9	230	22
	0.7	2.0	1.4	1.4	0.4	1.9	290	20
	1.3	2.0	1.7	1.7	0.5	2.4	400	21

TABLE 1. Summary of simulation parameters. The corresponding number of grid points are $(n_x, n_y, n_z) = (960, 96, 384)$ for $Ra \leq 0.4 \times 10^9$ and $(n_x, n_y, n_z) = (1200, 120, 480)$ for $Ra \geq 0.7 \times 10^9$. $T_s/(L_z/U_\Delta)$ and $T_s/\langle t_d \rangle$ are the total simulation sampling interval in terms of the free-fall velocity and droplet rise times, respectively.

The droplets are fully resolved using IBM for deformable interfaces and the interaction potential approach (de Tullio & Pascazio 2016; Spandan *et al.* 2017, 2018a). The simulations are also coupled in a so-called four-way manner, i.e. the simulation is capable to handle droplet-fluid forcing, fluid-droplet forcing, droplet-droplet collisions and droplet-wall collisions. Our numerical methodology differs from point-particle-type simulations with heat transport (e.g. Oresta *et al.* 2009): Since the droplets with diameter D (at the point of injection) are significantly larger than the turbulent Kolmogorov length-scale η , we therefore fully resolve the inhomogeneous hydrodynamic forces acting at the droplet interface. To illustrate this point, we wish to stress that $D/\eta \approx 7\text{--}19$ in our simulations. Here, $\eta \equiv (\nu^3/\varepsilon)^{1/4}$, where $\varepsilon \equiv \nu \langle (\partial u_i / \partial x_j)^2 \rangle$ is the volume-averaged turbulent kinetic energy dissipation rate. The key points of our IBM are summarised in § 2.1.

2.1. Numerical details

The liquid phase is solved using DNS by a staggered second-order accurate finite difference scheme and marched in time using a fractional-step approach (Verzicco & Orlandi 1996). We employ equal grid spacings in the x and y directions, whereas the

z direction is stretched using a Chebychev type clustering. The selected resolutions are constrained by considerations of three issues:

- (i) the resolution at the corner flow regions,
- (ii) the resolution at the bulk flow,
- (iii) minimum number of gridpoints per droplet diameter.

Concerning point (i), we based our estimate from the minimum resolution guidelines proposed for laminar-like thermal convection simulations (Shishkina *et al.* 2010). As a check, a coarser simulation with 20% less grid points results in Nu values that are within 0.5%, indicating good convergence for our resolution. For point (ii), we determined that $\max[\Delta x_i^\dagger \equiv \Delta x_i/\delta_\nu] \approx 2.4$ (details in table 1), where Δx_i are the grid spacings in each i th direction and $\delta_\nu \equiv \nu/u_\tau$ is the viscous length scale based on the shear velocity scale $u_\tau \equiv [\nu(d\bar{u}/dz)|_w]^{1/2}$. Point (iii) is closely related to point (ii): although the bulk resolutions are coarse, they are carefully selected such that $D/(\max[\Delta x_i]) \gtrsim 28$, comparable to other immersed boundary studies in turbulent flow with finite-size particles (Wang *et al.* 2019). Other numerical strategies are certainly possible, such as employing uniform grid spacings (Lu *et al.* 2005) or by eliminating walls in the simulations (Uhlmann & Chouippe 2017), however, these strategies are either limited by the Reynolds numbers, or can be computationally costly. The resolutions employed here are therefore a careful compromise for our values of droplet rise Reynolds numbers,

$$Re_d \equiv U_d D/\nu, \quad (2.7)$$

where U_d is the time-averaged vertical rise velocity of the droplet. Finally, to justify this point, we compare our IBM resolutions with the minimum resolution conditions for a flow over a rigid sphere (Johnson & Patel 1999). Given that our maximum droplet rise Reynolds number, $\max[Re_d] \approx 220$ (see figure 2), for an equivalent sphere Reynolds number, the dimensionless boundary layer thickness at its stagnation point is $\delta_{sp}/D \approx 1.13Re_d^{-1/2} \approx 0.08$ (Schlichting & Gersten 2000). Our simulation resolution assures that at least two grid points reside within the droplet boundary layer. It may be tempting to treat this grid resolution as inadequate, however, we emphasize that this estimate is not only based on the extreme boundary layer criterion at the stagnation point, it is also based on the maximum Re_d value and largest grid spacing in our setup. Our IBM resolution improves at lower Re_d (i.e. for thicker droplet boundary layers) and for finer near-wall grid spacings.

The dispersed phase is simulated with the IBM using a fast moving-least-squares algorithm (Spandan *et al.* 2017, 2018a). Two volume fractions are simulated: $\alpha = 5 \times 10^{-3}$ and 2×10^{-2} (see table 1). In addition to the sampling intervals for fluid simulations, $T_s/(L_z/U_\Delta)$, where $U_\Delta \equiv (g\beta\Delta L_z)^{1/2}$ is the free-fall velocity, the number of droplet flow-through cycles, $T_s/\langle t_d \rangle$ where $\langle t_d \rangle$ is the time-averaged droplet rise time, is also an important parameter. At least 20 droplet rise intervals are recorded for each simulation. Droplets that rise close to the top of the domain are removed and re-injected randomly at the bottom of the domain. This procedure ensures a constant droplet volume fraction and a uniform droplet spatial distribution. In addition, the interfacial temperature is set as the mean temperature of the immersed fluid.

For the droplet boundary conditions, we assume that the droplets have negligible thermal inertia and are surfactant-laden. The first assumption implies a small droplet Biot number, defined by $Bi \equiv hD/k$ where h is the heat transfer coefficient and k is the thermal conductivity of the droplet interface, so that the internal droplet temperature can be approximated by a uniform temperature in accordance with the lumped-capacitance model (Wang *et al.* 2017). Owing to deformation, individual droplet volumes can vary

slightly throughout the simulation, but fluctuate about a constant reference volume—this is the underlying model of the interaction potential approach. Effectively, the droplet boundary conditions are no-slip and impermeable for velocity, with a homogeneous time-dependent temperature at the interface (The thermal boundary conditions are discussed in §2.2). Indeed, for physical systems with surface-active impurities, droplet interfacial dynamics may be closely approximated by a no-slip interface (Jenny *et al.* 2004; Duineveld 1995). These simplified boundary conditions also have the added benefit that they can be handled easily from a numerical point-of-view, and hence, are computationally efficient given the size of the flow problem.

To quantify the droplet deformability, we define the Weber number, $We \equiv \rho_{\text{ref}} U_{\Delta}^2 D / \sigma$, which yields the ratio of inertia to capillary forces, where σ is the surface tension. In our simulation strategy, σ is not prescribed explicitly. Rather, an additional tuning step is performed to obtain a set of interaction potential constants such that $We \approx 3 \times 10^{-2}$, in accordance with the tuning criteria described in Spandan *et al.* (2017). It is emphasised that in order to simplify existing continuum models, this tuning step is a necessary and felicitous step in the implementation of our numerical model. After extensive precursor simulations and checks, we decided to simulate droplets at half the density of the fluid, i.e. $\hat{\rho} \equiv \rho_d / \rho_{\text{ref}} = 0.5$, which is within the numerical stability limit for explicit IBM time integration schemes (Schwarz *et al.* 2015). Another reason why the explicit formulation is typically favoured over implicit (i.e. strongly coupled) approaches for the fluid-structure interaction is also because of its computationally inexpensive nature. The detailed explanation of the methodology is, however, beyond the scope of this paper. For an in-depth discussion of the formulation, we refer readers to the paper of Spandan *et al.* (2017).

2.2. Model for thermally coupled droplets

For the lumped-capacitance model, two simplifying assumptions are made: (i) the droplets do not generate heat, and (ii) the internal temperature fields (and therefore interfacial temperature) of the droplets are uniform. Based on these assumptions, the interfacial droplet temperature is updated at every timestep according to

$$\frac{\partial \theta_b}{\partial t} = \left\langle -\frac{\kappa}{V_d} \oint_{S_d} \frac{\partial \theta}{\partial \mathbf{n}} \cdot \mathbf{n} \partial S_d \right\rangle_{S_d}, \quad (2.8)$$

where θ_b is the mean interfacial droplet temperature, V_d is the volume of the droplet, S is the droplet surface area and \mathbf{n} is the outwardly-directed unit normal. $\langle \cdot \rangle_S$ denotes the surface-averaged quantity. The droplet surface temperature is initialised as the mean surface temperature at its injected location. After injection, the droplets rise and deform with respect to their original state (a sphere with diameter D), but do not significantly change in volume. Our model is therefore simpler than other numerical models with thermal coupling, for instance, studies that consider droplet growth at the boiling limit (e.g. Oresta *et al.* 2009; Lakkaraju *et al.* 2011) or models that rely on droplets with a constant geometry (e.g. Wang *et al.* 2017). Our code was extensively validated in a recent study for convection-dominated dissolution of droplets (Chong *et al.* 2019).

2.3. Derivation of the droplet Rayleigh number

In addition to the control parameters defined in (2.4), we introduce the droplet Rayleigh number, Ra_d , to quantify the droplet driving. It is defined as

$$Ra_d \equiv \frac{\alpha g L_z^3}{\hat{\rho} \nu \kappa}, \quad (2.9)$$

which is conveniently derived from scaling arguments of the governing equations.

Following the definition of IBM for deformable interfaces/fluid-structure interaction, the droplet interface is represented by a network of nodes evolved by the interaction potential model (de Tullio & Pascazio 2016; Spandan *et al.* 2017). The equation of motion for each node, e , moving with velocity \mathbf{u}_e is

$$\frac{d\mathbf{u}_e}{dt} = \mathbf{F}^h + \mathbf{F}^g + \mathbf{F}^i. \quad (2.10)$$

In (2.10), the terms are made dimensionless with the unit length L_z and free-fall velocity U_Δ . The forces contributing to the right-hand-side of (2.10) are the hydrodynamic loads \mathbf{F}^h , buoyancy \mathbf{F}^g and internal forces \mathbf{F}^i , where

$$\mathbf{F}^h = \frac{L_z}{\hat{\rho}V_e U_\Delta^2} \int_S \boldsymbol{\tau} \cdot \mathbf{n} dS \quad \text{and} \quad \mathbf{F}^g \equiv \left(1 - \frac{1}{\hat{\rho}}\right) \frac{L_z}{U_\Delta^2} \mathbf{g}. \quad (2.11a,b)$$

In (2.11a), V_e is the volume of the node, but lacks a physical definition because the definition of the thickness of a liquid-liquid interface is not straightforward. To overcome this, following Spandan *et al.* (2017), we treat V_e as a free parameter and fix $V_e = 1$. The model parameters for the internal forces \mathbf{F}^i are then correspondingly tuned. \mathbf{F}^i represents the surface forces acting on the nodes of the discretised droplet surface and is based on the principle of minimising the potential energy of immersed interface. Under external hydrodynamic loads, the network of nodes deform and stores potential energy into the system. The potential energy is subsequently converted to surface forces by differentiating the potentials with respect to the displacements of each node. The details of the individual potentials are described in Spandan *et al.* (2017).

We focus on the second term \mathbf{F}^g in (2.11b). Since (2.11b) represents the contribution from an isolated droplet and we are interested to define a parameter for collective droplet effects, it would be reasonable to include the volume fraction parameter, α . Therefore, for $\hat{\rho} < 1$, we define,

$$F_\alpha^g \sim \frac{\alpha g L_z}{\hat{\rho} U_\Delta^2} =: \frac{Ra_d}{Ra}, \quad (2.12)$$

which quantifies the relative dominance of droplet driving to thermal driving.

Other dimensionless parameters similar to Ra_d/Ra have also been proposed for different flow configurations, but these require *a priori* knowledge of the dispersed phase dynamics and/or flow statistics. For example, Climent & Magnaudet (1999) proposed the Rayleigh number expression, $Ra_{CM} \equiv \rho g \alpha H^3 / (\nu U_b)$ (H is the height of the liquid layer and U_b is the relative rise velocity of the bubble), to quantify bubble-induced convection. Based on the notion of pseudo-turbulence (Lance & Bataille 1991), which is defined as the fluctuating energy induced by the passage of bubbles under non-turbulent conditions, van Wijngaarden (1998) proposed the so-called bubbance parameter $b \equiv (1/2)U_b^2 \alpha / u_0^2$ (u_0 is the vertical velocity fluctuations of background turbulence). Since Ra_d/Ra is a natural control parameter for VC with light droplets, we therefore use this ratio as input for our simulations. Note that Ra_d is constant for a given α and therefore Ra_d/Ra reduces with increasing Ra (this is equivalent to an *increase* in Froude number with increasing Ra). To make the simulations of the fluid-structure interaction tractable, we also run the simulations at $g/200$. The resulting Ra_d/Ra is $5 \times 10^{-4} - 5 \times 10^{-5}$ for $\alpha = 5 \times 10^{-3}$ and $2 \times 10^{-3} - 2 \times 10^{-4}$ for $\alpha = 2 \times 10^{-2}$.

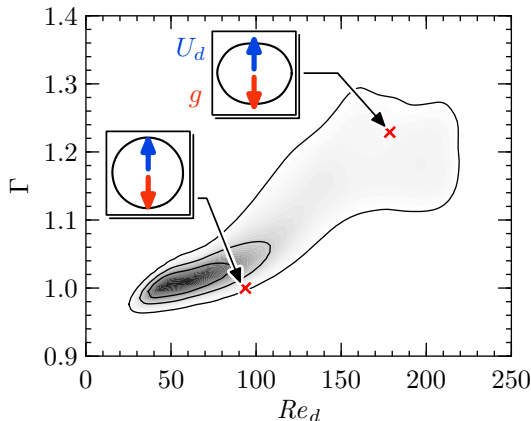


FIGURE 2. Joint p.d.f. of droplet deformations characterised by Γ versus the droplet rise Reynolds number, Re_d , averaged over all cases. Outermost contour level is 0.03 and the contours are spaced 0.06 apart. Inset plots show representative two-dimensional droplet shapes for two Re_d values. Also shown are the directions of the droplet rise velocity U_d and gravity g .

3. Droplet influence on flow statistics and profiles

In this section, we analyse the results for $0 \leq \alpha \leq 2 \times 10^{-2}$, starting with a discussion of the droplets statistics.

3.1. Distribution of droplet aspect ratio versus bubble Reynolds number

From our simulations, the maximum droplet Reynolds number is $Re_d \approx 220$ and its time-averaged value is, $\langle Re_d \rangle \approx 100$. As the droplets rise, they undergo deformation from the interfacial hydrodynamic loads. In figure 2, we characterise the deformation of the droplets in our simulations using the aspect ratio, Γ , of the major to minor axes, which are determined by fitting two-dimensional Fourier descriptors (Duineveld 1995; Lunde & Perkins 1998) to the projected droplet outlines in the xy - and xz -plane. The joint probability density distribution in figure 2 shows that the droplets undergo moderate deformation between $\Gamma \approx 1$ to $\Gamma \approx 1.3$, agreeing with the relatively small We values. Visual inspections of the instantaneous shapes (insets of figure 2) show that the spherical droplet loses its fore-aft symmetry, with the front of the droplet becoming flatter than the back. Due to the relatively moderate Re_d values, we do not observe droplet path instabilities throughout our simulations.

3.2. Profiles of mean vertical velocity and temperature

Now, we turn our focus to the flow statistics. To establish a baseline, we first analyse the influence of the droplets on the mean flow profiles of VC.

Figure 3 shows the mean vertical velocity and temperature profiles plotted versus z (Note that all length scales have been made dimensionless with L_z). Without droplets, the mean profiles are anti-symmetric about the channel centre-line (figure 3a,d). The cell centre is stably stratified (figure 4d) with $d\bar{\theta}/dz|_{z=0.5} = 0$ and $\bar{u}|_{z=0.5} = 0$. Therefore, unlike the doubly-periodic VC setup (Ng *et al.* 2015, 2017), there is no persistent mean shear in the bulk of the flow. For $\alpha > 0$ and for both coupling cases, the mean vertical velocity profiles are asymmetric with a much stronger downward velocity magnitudes near the cooler walls (figures 3b,c). The difference between the maxima and minima of \bar{u} is largest for the smallest Ra , indicating that the droplet forcing is strongest.

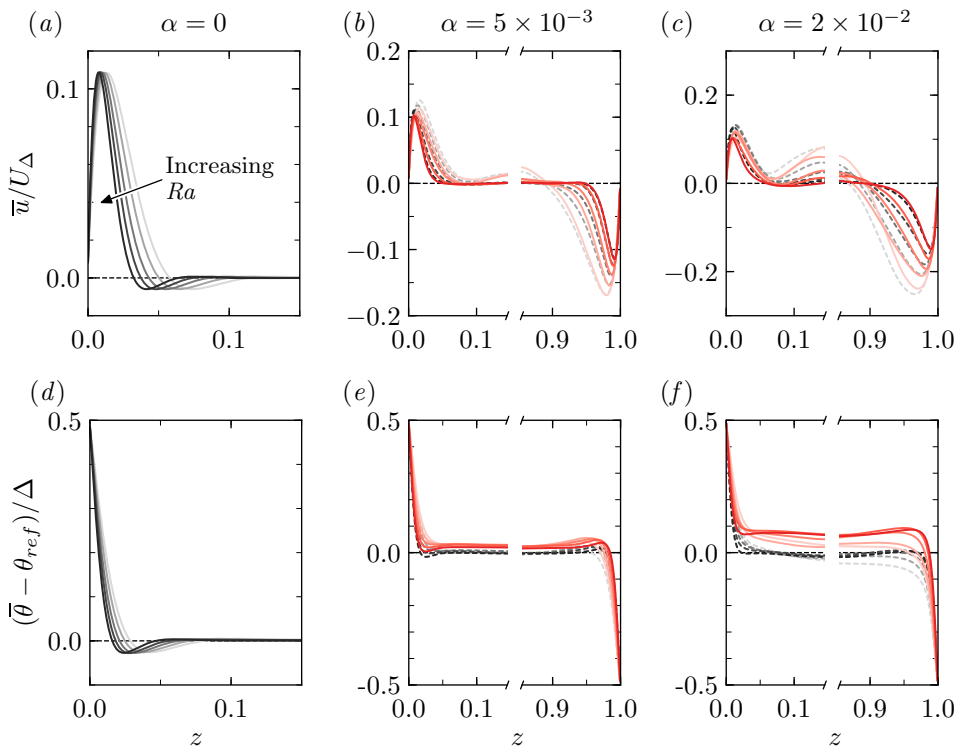


FIGURE 3. Mean profiles as a function of horizontal location z : (a-c) vertical velocity, (d-f) temperature. (a,d) $\alpha = 0$, (b,e) $\alpha = 5 \times 10^{-3}$, and (c,f) $\alpha = 2 \times 10^{-2}$. For $\alpha = 0$, only the left half of the profiles are shown since the profiles are antisymmetric about the vertical centreline. Dashed grey curves represent mechanical coupling only. Solid red curves represent mechanical and thermal coupling. Darker curves represent higher Ra .

The mean temperature profiles (figures 3e,f) also exhibit asymmetries. For $\alpha = 5 \times 10^{-3}$ and at the lowest Ra , the temperature profiles for both coupling cases are relatively constant and do not exhibit any undershoot, which is observed for $\alpha = 0$ in figure 3(d) at $z \approx 0.04$. However, at higher Ra , the profiles now bear some resemblance to the cases when $\alpha = 0$, corroborating the notion that thermal driving increasingly dominates. Here, we note that although $\bar{\theta} > \theta_{\text{ref}}$ in the bulk, the globally averaged temperature field $\langle \theta \rangle_t$ is statistically stationary within 0.5% for all cases. In the bulk region ($0.2 \leq z \leq 0.8$), we obtain $d\bar{\theta}/dz|_{\text{bulk}} \approx 0$. Based on these results, the influence of the light droplets is seemingly most pronounced at the vertical boundaries as compared to the bulk.

3.3. Profiles of mean horizontal velocity and temperature

Figure 4 shows the mean horizontal velocity and temperature profiles plotted versus x . When $\alpha = 0$, the velocity profiles are antisymmetric (figure 4a) and the temperature profiles are constant for all Ra (figure 4d). When $\alpha > 0$, the antisymmetries are destroyed: for $\alpha = 0.5 \times 10^{-2}$, the horizontal velocities are larger at the top wall (figure 4b), whereas for $\alpha = 2 \times 10^{-2}$, the horizontal velocities are larger at the bottom wall (figure 4c). The source for the asymmetry can be traced to passage of droplets entering the bottom or leaving the top of the domain: at the lower boundary, the droplets which have near zero velocity block the horizontal flow causing the fluid to accelerate around the droplets. At

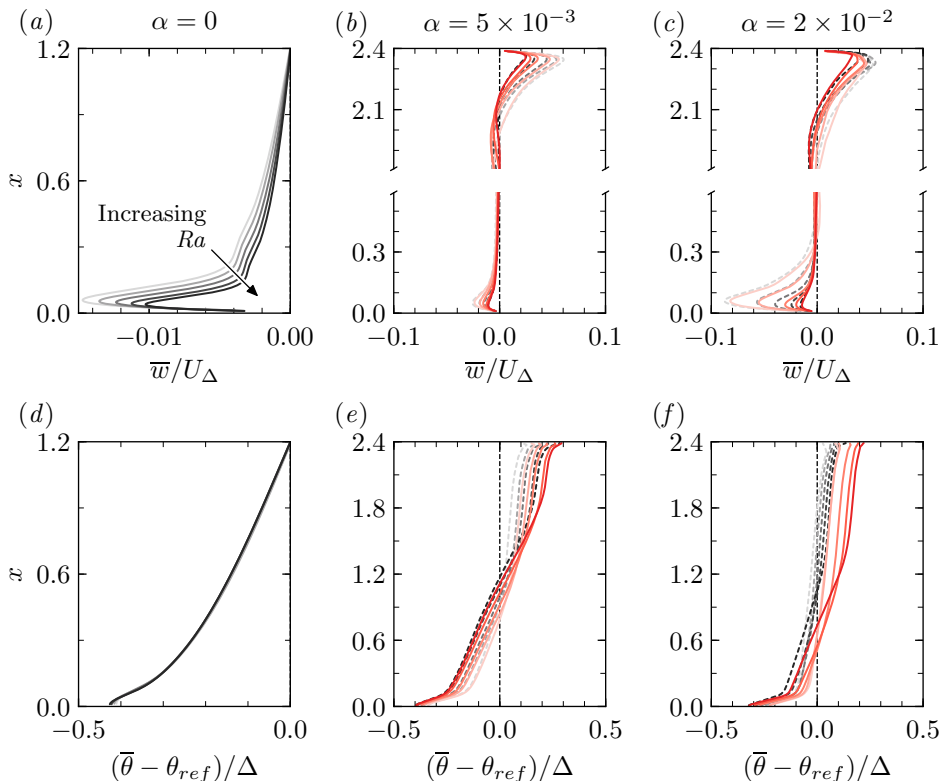


FIGURE 4. Same as figure 3, but now for the mean profiles as a function of the vertical spatial variable x : (a-c) \bar{w}/U_Δ , (d-f) $(\bar{\theta} - \theta_{ref})/\Delta$. For $\alpha = 0$, only the velocity profiles between $0 \leq x \leq 1.2$ are shown since the profiles are antisymmetric about the horizontal centreline. Colour legends are the same as figure 3.

the upper boundary, the droplets exit the domain at terminal velocity, and the entrained fluid impinges on the upper wall. Both mechanisms trigger intermittent intrusions of hotter and colder fluid at the upstream corners of the thermal boundary layers at the vertical walls. Since the blockage factor is higher for the $\alpha = 2 \times 10^{-2}$ cases, the magnitude of the mean horizontal velocities are larger at $x \lesssim 0.3$ as compared to the $\alpha = 5 \times 10^{-3}$ cases.

For the temperature profiles, we note an overall weakening of the stable stratification at higher α (figures 4e and f), with the bulk mean temperatures $\bar{\theta} \rightarrow \theta_{ref}$. The relatively uniform value of $\bar{\theta}$ for the most part of x indicates strong mixing of the thermal field with increasing α .

3.4. r.m.s. profiles of vertical velocity and temperature

The root-mean-square (r.m.s.) of the fluctuating quantities are plotted in figure 5 for all cases as a function of horizontal distance z . Here, we define $(\cdot)'_{rms} \equiv [(\overline{(\cdot)^2})^{1/2}]$. When $\alpha = 0$ (figure 5a,d), both u'_{rms} and θ'_{rms} exhibit near wall peaks and are symmetrical about the channel-centreline.

When $\alpha > 0$, the bulk velocity fluctuations $u'_{bulk,rms} > 0$ as a direct result of droplet induced liquid fluctuations. Interestingly, $u'_{bulk,rms}$ at lower Ra values are much larger than at higher Ra , which highlights the larger influence of droplet forcing on the flow at

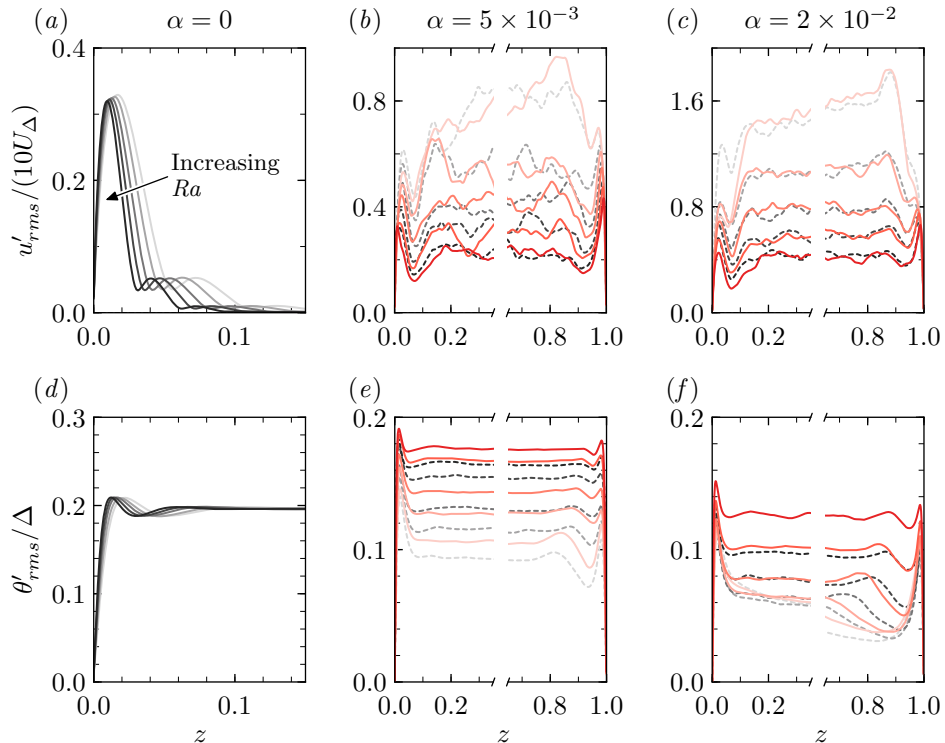


FIGURE 5. Same as figure 3, but now for the r.m.s. statistics as a function of z : (a-c) $u'_{rms}/(10U_{\Delta})$, (d-f) θ'_{rms}/Δ . For $\alpha = 0$, only the left half of the profiles are shown since they are antisymmetric about the vertical centreline. Colour legends are the same as figure 3.

lower Ra . The u'_{rms} profiles also exhibit slight asymmetry with values tending to be larger closer to the colder wall as compared to the hotter wall. This asymmetry is consistent with the notion of a more intermittent colder downwards flow caused by the disruption of the large-scale circulation by the droplet passage, as discussed in §3.2.

For θ'_{rms} , the magnitudes in the bulk for $\alpha > 0$ (figures 5e,f) tend to be lower than for the case when $\alpha = 0$ (figure 5d), where $\theta'_{rms,bulk} \approx 0.2$. With thermal coupling, the θ'_{rms} profiles are typically slightly larger than without thermal coupling and counteracts the mechanical agitation by the droplets. This effect can be explained by the thermal exchange of the droplet and the surrounding liquid which induces local thermal fluctuations. Therefore, both the mechanical agitation at larger α and the thermal coupling of the droplets contribute to the bulk mixing of the thermal field.

3.5. Scaling of Nusselt and Reynolds numbers versus Rayleigh number

In figure 6, we present the scaling of the Nu and Re versus Ra . Here, we employ the wind-based Reynolds number, $Re \equiv \bar{u}_{max}L_z/\nu$ as a measure of the large scale circulation.

When $\alpha = 0.0$ (solid circles, figure 6), we find that $Nu \sim Ra^{0.25 \pm 0.003}$ and $Re \sim Ra^{0.50 \pm 0.002}$ which are in agreement with the $Nu \sim Ra^{1/4}$ and $Re \sim Ra^{1/2}$ analytical predictions for laminar boundary layer-dominated VC (Shishkina 2016). For pure mechanical coupling (open triangles), the Nu trends exhibit steeper slopes and from a least-square fit to a power-law, we obtain $Nu \sim Ra^{0.29 \pm 0.02}$ for $\alpha = 5 \times 10^{-3}$ and $Nu \sim Ra^{0.26 \pm 0.04}$ for $\alpha = 2 \times 10^{-2}$. In contrast, the Re slopes are less steep and from a least-square fit

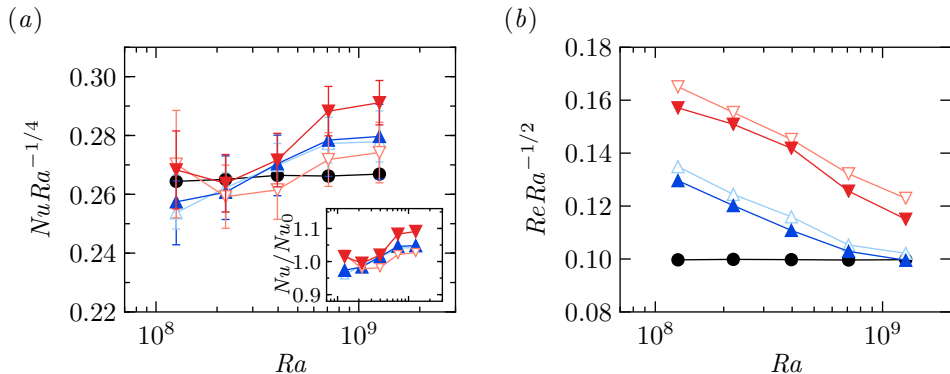


FIGURE 6. (a) Compensated Nu versus Ra , and (b) compensated Re versus Ra . Inset of (a): ratio of $Nu|_{\alpha>0}$ to $Nu|_{\alpha=0}$. Solid black symbols are DNS data for $\alpha = 0$. Upwards-pointing blue triangles are for $\alpha = 5 \times 10^{-3}$ cases and downwards-pointing red triangles are for $\alpha = 2 \times 10^{-2}$. Open triangles denote mechanical coupling only and filled triangles denote both mechanical and thermal coupling. The Nu versus Ra and Re versus Ra scalings for $\alpha = 0$ are consistent with analytical predictions for VC driven by laminar boundary layers, i.e. $Nu \sim Ra^{1/4}$ and $Re \sim Ra^{1/2}$ at constant Pr (Shishkina 2016).

to a power-law, we obtain $Re \sim Ra^{0.38 \pm 0.03}$ for $\alpha = 5 \times 10^{-3}$ and $Re \sim Ra^{0.37 \pm 0.02}$ for $\alpha = 2 \times 10^{-2}$. When both mechanical and thermal coupling are enabled (filled triangles), we obtain $Nu \sim Ra^{0.29 \pm 0.02}$ and $Re \sim Ra^{0.38 \pm 0.03}$ for $\alpha = 5 \times 10^{-3}$, and $Nu \sim Ra^{0.29 \pm 0.04}$ and $Re \sim Ra^{0.36 \pm 0.06}$ for $\alpha = 2 \times 10^{-2}$. When comparing the coupling cases, the effective scaling for Nu and Re is largely unaffected. However, by including thermal coupling, the temperature field is distributed more efficiently and so, the magnitude of the heat transport is increased.

As a direct comparison for Nu , the ratio $Nu/Nu_{\alpha=0}$ is shown in the inset of figure 6(a) and the values range from 0.95 to 1.1. Some caution is warranted here when interpreting the ratios. Because of the rather large variations of $NuRa^{-1/4}$ as shown in the figure, we cannot conclusively claim that there exist a decrease in Nu at low Ra . However, we can link the variations of the ratios to the different manner in which the droplets locally influence the wall heat fluxes and wall shear stresses. The local influences are quantified and discussed in § 4 and in § 5.

Now, we focus on the Re trends. For $\alpha > 0$, the Re values tend to be larger than for the $\alpha = 0$ case and this is consistent with the response of the VC flow due to the passage of the droplets across the top and bottom boundary layers. As the droplets cross the horizontal boundary layers, the large-scale circulation of the background VC flow is continuously disrupted, triggering horizontal intrusions of warmer fluid at the top wall and cooler fluid at the bottom wall (peaks in mean horizontal velocities in figures 4b and c), similar to the intrusions observed in transient VC in a square cavity (Patterson & Imberger 1980; Armfield & Patterson 1991). For $\alpha = 5 \times 10^{-3}$, at the higher Ra -values, the Re -values tend to approach the Re values for $\alpha = 0$. This incipient trend suggests that the droplet driving is no longer dominant at this part of the parameter space as compared to the $\alpha = 2 \times 10^{-2}$ case.

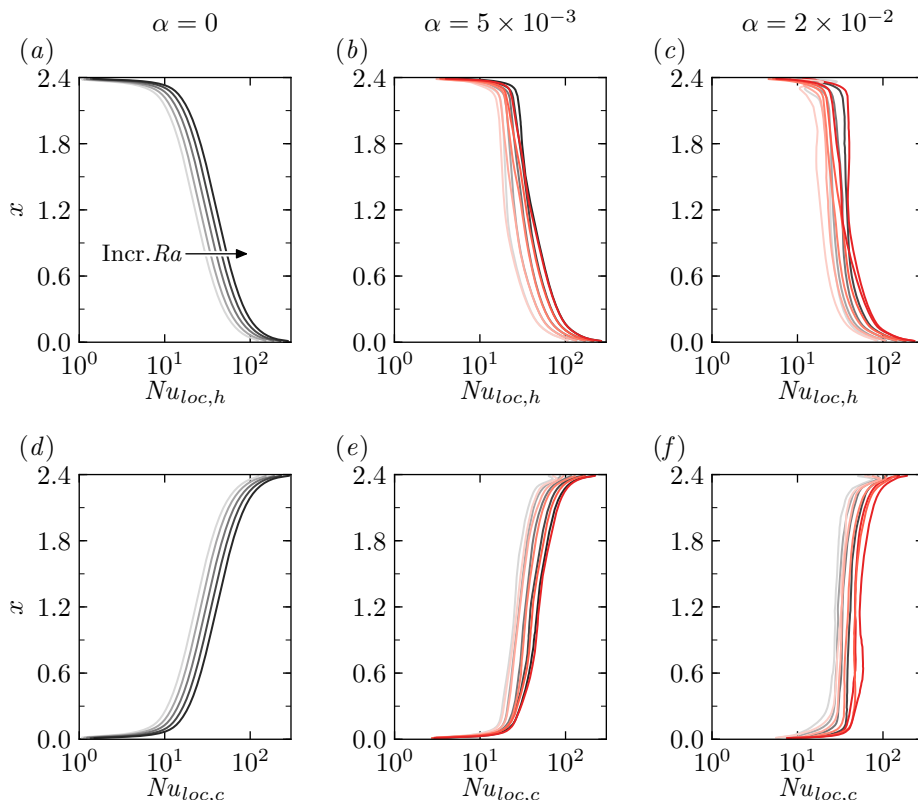


FIGURE 7. Profiles of Nu_{loc} plotted as a function of x at the hot wall (a-c), and the cold wall (d-f). Colour legends are the same as figure 3.

4. Droplet influence on local Nusselt number

In this section, we link the Nu versus Ra variations discussed in § 3.5 to the changes in the local Nusselt number evaluated at the hot and cold walls. We define the local Nusselt number as $Nu_{loc} \equiv f_{w,loc} L_z / (\Delta \kappa) = [\partial \bar{\theta}(x) / \partial z]_w / (\Delta L_z)$, which is the local dimensionless temperature gradient evaluated at $z = 0$ and L_z . The trends are shown in figure 7 as function of x .

From figure 7, Nu_{loc} are larger in the upstream of the vertical boundary layers, that is $x \lesssim 1.2$ for figures 7(a-c) and $x \gtrsim 1.2$ for figures 7(d-f). Here, the larger values of Nu_{loc} simply reflect the thinner thermal boundary layers developing from the corners of the domain. For $\alpha = 0$, Nu_{loc} monotonically decreases as the boundary layer develops and is consistent across the Ra range. However, the trends vary considerably for $\alpha > 0$. For example, relative to the $\alpha = 0$ cases, (i) $Nu_{loc,h}$ becomes lower for $x \lesssim 1.2$, and (ii) for $\alpha = 2 \times 10^{-2}$, both $Nu_{loc,h}$ and $Nu_{loc,c}$ are roughly constant for $0.6 \lesssim x \lesssim 1.8$. Since these changes directly reflect the thermal boundary layer thicknesses, we can conclude that the droplets not only influence the bulk statistics as shown in § 3, but would also influence the local thermal boundary layers.

To emphasise the changes in Nu_{loc} , we plot the ratio of Nu_{loc} and $Nu_{loc,0}$ in figure 8. ($Nu_{loc,0}$ is Nu_{loc} computed for the $\alpha = 0$ cases). The corresponding wall-areas for Nu_{loc} are also shown in the insets, with reduced- Nu_{loc} values denoted by left-pointing open triangles, and increased- Nu_{loc} values denoted by right-pointing solid triangles. For

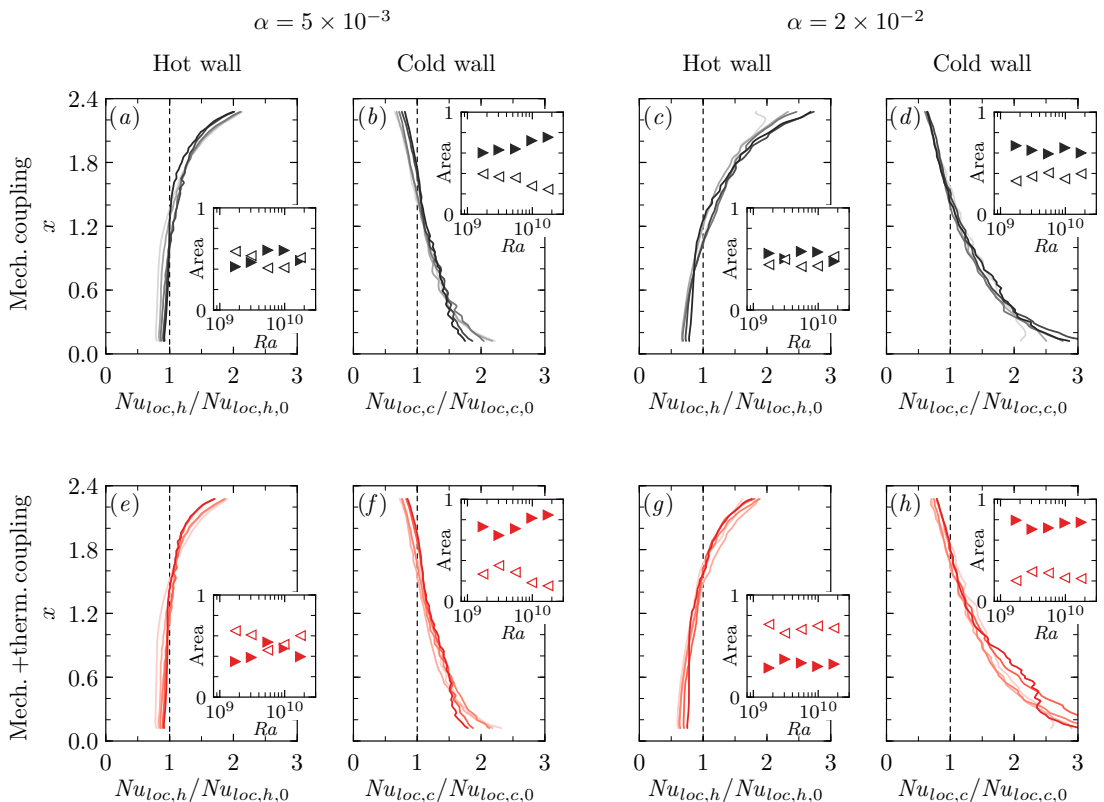


FIGURE 8. Ratio of Nu_{loc} to $Nu_{loc,0}$, which is the case for $\alpha = 0$. The corresponding wall-areas of the ratios versus Ra are shown in the inset: wall-areas with reduced Nu_{loc} are denoted by left-pointing open triangles, and increased Nu_{loc} by right-pointing solid triangles. Darker curves represent higher Ra .

$\alpha = 5 \times 10^{-3}$, the decreased $Nu_{loc,h}$ can be clearly seen for all Ra and $x/L_x \lesssim 1.2$ (figures 8a,e). This decreasing behaviour can also be observed for $\alpha = 2 \times 10^{-2}$, although the corresponding wall-area with decreased $Nu_{loc,h}$ is smaller for the mechanically coupled case (see figure 8c and the inset plot). The decreased $Nu_{loc,h}$ for the $\alpha = 5 \times 10^{-3}$ case overwhelms the increased $Nu_{loc,c}$ for $x/L_x \lesssim 1.2$, with the lowest Ra cases being most strongly influenced, as previously shown in figure 6. In contrast, $Nu_{loc,c}$ is significantly increased for $\alpha = 2 \times 10^{-2}$ and $x \lesssim 1.2$ by roughly a factor of 1.5 times (figures 8d,h). Based on the much stronger droplet driving for $\alpha = 2 \times 10^{-2}$, $Nu|_{\alpha=2 \times 10^{-2}}$ is increased by about 5% for the lowest Ra relative to $Nu|_{\alpha=5 \times 10^{-3}}$.

For the different distributions of Nu_{loc} in figures 7 and 8, we emphasize that they are non-universal phenomena for the flow problem considered since the mechanism of the changes rely on the strength of the droplet driving, Ra_d . These changes therefore cannot be trivially determined *a priori*. What can be discerned from the current results is that the droplets influence the bulk flow (as seen in the mean and r.m.s. statistics in figures 3 to 5), the near-wall flow and the large-scale circulation of VC. Different mechanisms in these regions compete and the prevailing mechanism(s) would presumably determine the heat transport of the setup.

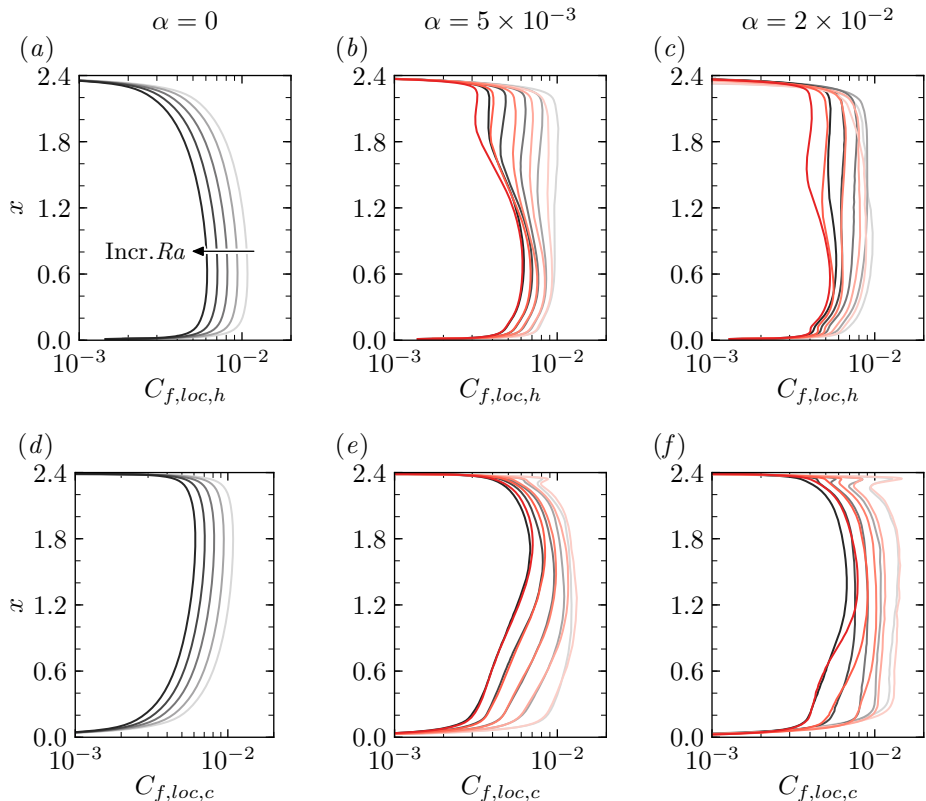


FIGURE 9. Similar to figure 7, but now for the local skin-friction coefficient $C_{f,loc}$. Colour legends are the same as figure 3.

5. Droplet influence on local skin-friction coefficient

Unlike Rayleigh–Benárd convection, the thermal boundary layers in VC are sheared by a mean wind with a constant direction that is predetermined by the boundaries (Ng *et al.* 2015). Therefore, to quantify the influence of the droplets on wind-shearing, we plot the local skin-friction coefficient $C_{f,loc}$ versus x in figure 9. Here, $C_{f,loc} \equiv 2\tau_w(x)/U_{\Delta}^2$, where $\tau_w(x) \equiv \sqrt{\mu \partial \bar{u}(x)/\partial z|_w}$ is the wall shear stress. Similar to the idea of figure 8, the relative changes in the local skin-friction coefficients are plotted in figure 10.

For $\alpha = 0$, $C_{f,loc}$ is largest at wall heights that are close to the upstream of the developing boundary layer. However, when $\alpha > 0$, $C_{f,loc}$ is roughly constant for the most part of x at low Ra . Two points can be made from the distributions of $C_{f,loc}$. First, the roughly uniform distribution of $C_{f,loc}$ at low Ra for $\alpha > 0$ imply that the droplet driving dominates the mean wind of VC and, on a mean sense, homogenizes the viscous boundary layer particularly at the hot wall. Second, the distributions of $C_{f,loc}$ are not symmetric at the hot and cold walls (for example, $\max[C_{f,loc,c}] > \max[C_{f,loc,h}]$) as compared to the $\alpha = 0$ case (figure 8a and d). One possible explanation of this asymmetry can be made by observing the rising direction of the droplets: At the cold wall, the droplets oppose the downwards flow whereas at the hot wall, the droplets aid the upwards flow. Coupled with the asymmetry of the mean horizontal velocity profiles in figure 4, the resulting viscous boundary layer becomes thinner at the cold wall, and a larger $C_{f,loc}$ results.

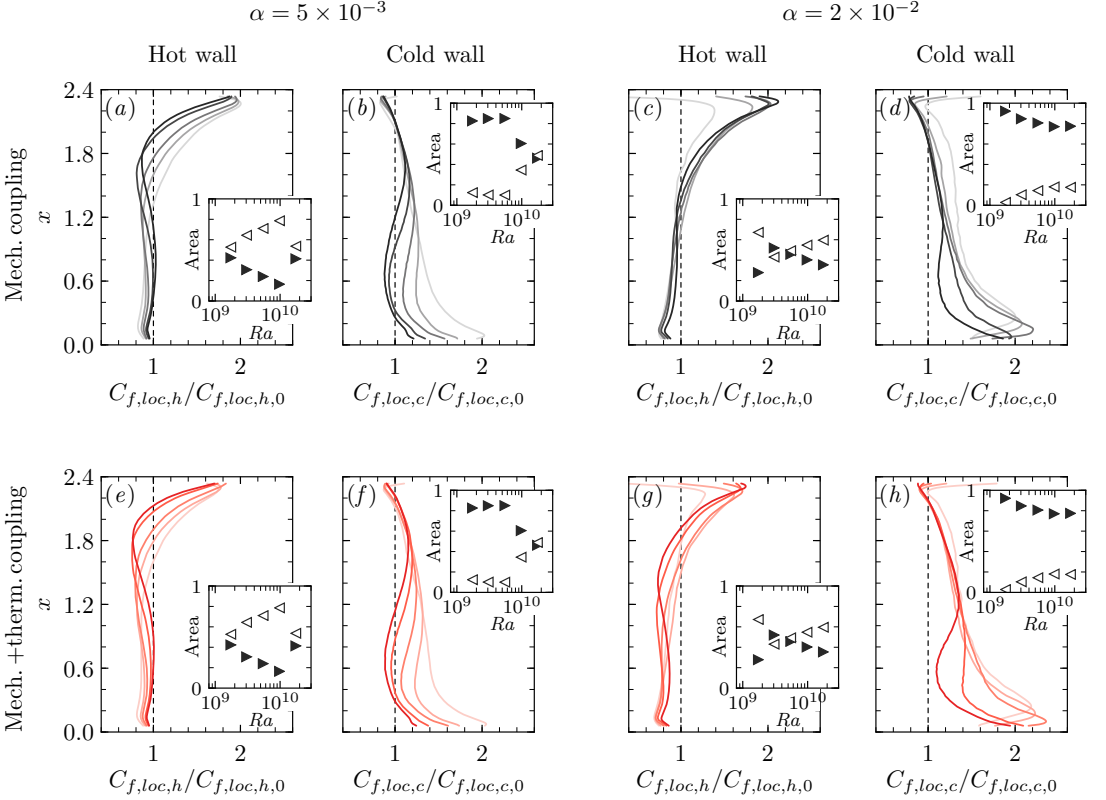


FIGURE 10. Similar to figure 8, but now for the local skin-friction coefficient $C_{f,loc}$. The corresponding wall-areas of the ratios versus Ra are shown in the inset: wall-areas with reduced $C_{f,loc}$ are denoted by left-pointing open triangles, and increased $C_{f,loc}$ by right-pointing solid triangles. Colour legends are the same as figure 8.

However, this conjecture may not hold at higher Ra cases because the viscous boundary layers eventually become much thinner and closer to the walls. As a result, at sufficiently high Ra , the influence of droplets presumably diminishes with increasing distance from the edge of the viscous boundary layers, eventually yielding to the dynamics of thermal driving.

When compared with $C_{f,loc,0}$ (figure 10), we find larger values of $C_{f,loc}$ in concomitant regions with larger values of Nu_{loc} in figure 8. Interestingly, whilst Nu_{loc} is relatively insensitive to Ra (see figure 8), the wall-height distributions of $C_{f,loc}$ exhibit a strong non-monotonic behaviour which depends on Ra , α and whether the cold or hot wall is considered. Therefore, it appears that $C_{f,loc}$ is more sensitive to the droplets induced agitation as compared to Nu_{loc} . These results provide a strong indication that the light droplets interact with VC flow in a non-universal manner.

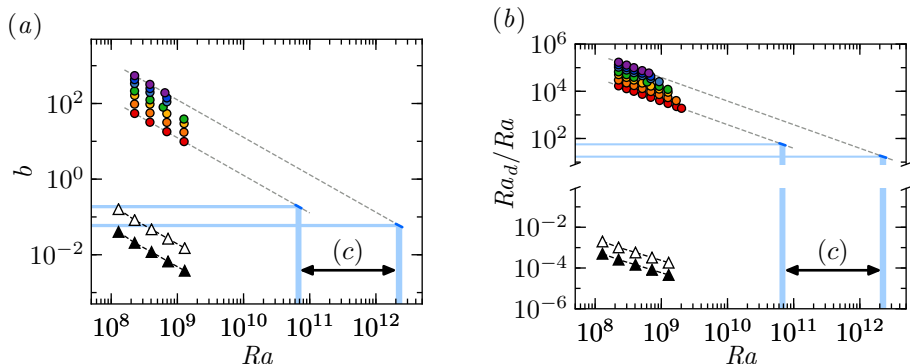


FIGURE 11. Plots of (a) bubble parameter, b , versus Ra , and (b) Ra_d/Ra versus Ra . The range of $Ra_c(\alpha)$ values from the experiments of Gvozdić *et al.* (2018) are marked in (c). Present DNS results are solid triangles for $\alpha = 5 \times 10^{-3}$ and open triangles for 2×10^{-2} . Experimental values (circles, red to purple fill denoting increasing α) are estimated from the physical properties reported in Gvozdić *et al.* (2018). In (a), only a subset of the experimental values are estimated by assuming values of u_0 to our DNS results. The intersect of (c) and the dashed grey lines, i.e. $b \sim Ra_c^{-1}$ and $Ra_d/Ra \sim Ra_c^{-1}$, are approximations of b and Ra_d/Ra for the lowest and highest α from laboratory experiments.

6. Light droplets versus bubbles - a comparison to experiments by Gvozdić *et al.* (2018)

In this section, we discuss several aspects of the physical parameters in our simulations, which distinguish our findings from the laboratory results of bubbly VC by Gvozdić *et al.* (2018).

A crucial difference between our investigation and the experiments is that $\hat{\rho} = 0.5$ in our simulations (corresponding to light droplets) whereas $\hat{\rho} \approx 10^{-3}$ in their experiments (corresponding to air bubbles in water). Clearly, the large differences in the density ratios play a role and this is reflected in our simulations. For example, the mean temperature in the bulk region of our simulations have approximately zero gradient (figure 3), whereas the mean temperature in the bulk region of the experiments have a finite gradient (see figure 9(a) of their paper), indicating a much stronger mixing of the thermal field by the bubbles as compared to light droplets. Furthermore, the values of Nu for VC with light droplets is within 10% of the Nu values without droplets (figure 6), whereas in the laboratory experiments of Gvozdić *et al.* (2018), Nu can be larger by up to 20 times with bubbles than without and remain Ra -independent for their investigated parameter range. Therefore, we conclude that the background VC flow remains relatively dominant even with influence of light droplets, and this is reflected in the non-universal distributions of the local heat transport and skin-friction coefficients shown in figures 8 and 10.

The strength of the bubble-induced agitation versus droplet-induced agitation can also be quantified *a posteriori* using the bubble parameter,

$$b \equiv U_b^2 \alpha / u_0^2, \quad (6.1)$$

(cf. Lance & Bataille 1991; van Wijngaarden 1998; Rensen *et al.* 2005; Alm eras *et al.* 2017), which defines the ratio of energy produced by a bubble swarm, i.e. $U_b^2 \alpha$, and the energy of the background turbulence without bubbles, i.e. u_0^2 . Note that a prefactor of 1 is chosen for (6.1), which is different to previous definitions which employ a prefactor of 1/2 (based on the added mass coefficient, cf. Rensen *et al.* 2005), however the present

discussions are still valid. We define U_b as the mean bubble or droplet rise velocity and u_0 as the maximum of the mean vertical velocity of the single phase flow at the half-height of the domain. Next, we estimate b for our DNS and for the experiments by Gvozdić *et al.* (2018).

Since we have the full information from our DNS, the calculation of b is straightforward. For the laboratory experiments, u_0 was not recorded and so, invoking dynamic similarity, we estimate the values using our DNS results at matched Ra . U_b is assumed to be 0.34 m s^{-1} for the laboratory experiments. The values of b are plotted in figure 11(a). From the figure, we find that $O(10^{-3}) \lesssim b \lesssim O(10^{-1})$ for our DNS whereas $O(10^1) \lesssim b \lesssim O(10^3)$ for the experiments. The much smaller magnitude of b for our DNS clearly indicates that light droplets produce much lower kinetic energy compared bubbles. Also, b decreases with increasing Ra and implies that the kinetic energy of the background flow will eventually dominate the (constant) injection of kinetic energy by the dispersed phase. Based on the same idea, we compare the ratio of Ra_d/Ra for our DNS and the experiments in figure 11(b). From the figure, we observe a similar scale separation and decreasing trend with increasing Ra : The values are $O(10^{-5}) \lesssim Ra_d/Ra \lesssim O(10^{-3})$ for our DNS and $O(10^3) \lesssim Ra_d/Ra \lesssim O(10^5)$ for the experiments, confirming that the bubble driving is indeed a stronger driving mechanism than light droplets.

It is useful for applications such as in chemical mixing to have an estimate of the parameter space for b or Ra_d/Ra where the driving by background turbulence eventually dominates bubble driving. For the laboratory experiments with bubbly VC, Gvozdić *et al.* (2018) estimated this parameter space by defining a critical Rayleigh number, Ra_c , as follows: First, an effective power-law trend of $Nu \sim Ra^{0.33}$ is obtained from the single phase experiments. Then, observing that the Nu trends are insensitive to Ra for $5 \times 10^{-3} \lesssim \alpha \lesssim 5 \times 10^{-2}$ (cf. figure 12 of Gvozdić *et al.* 2018), the $Nu \sim Ra^{0.33}$ and constant Nu trends are extrapolated to higher Ra values. The intersection of these curves are defined as Ra_c , where $7 \times 10^{10} \lesssim Ra_c(\alpha) \lesssim 2 \times 10^{12}$ for the α values investigated. The range of Ra_c values are marked in figure 11(c).

We can now directly extrapolate the trends of b and Ra_d/Ra to the Ra_c values. From least-square fits, the effective power laws are $b \sim Ra^{-1}$ and $Ra_d/Ra \sim Ra^{-1}$. Therefore, the extrapolated values are $b \sim Ra_c^{-1}$ and $Ra_d/Ra \sim Ra_c^{-1}$, visually marked by the blue patches in figure 11. For illustration purposes, only the $\alpha = 5 \times 10^{-3}$ and 5×10^{-2} are drawn and an allowance of $Ra_c \pm 10\%$ was employed to compute the extrapolation. The corresponding values are $(b, Ra_d/Ra)|_{\alpha=5 \times 10^{-3}} \approx (0.2, 60)$ and $(b, Ra_d/Ra)|_{\alpha=5 \times 10^{-2}} \approx (0.06, 18)$. These values suggest that the VC flow will dominate bubble-induced liquid agitation at $b \lesssim O(10^{-1})$ and $Ra_d/Ra \lesssim O(100)$. We note that our dataset for $\alpha = 2 \times 10^{-2}$ coincide with this regime for $b|_{\alpha=5 \times 10^{-2}}$ (lower horizontal blue line in figure 11a), however, since the boundary layer dynamics are still dominant for our configuration, it suggests that $\hat{\rho}$ is an additionally important parameter when characterising bubbly turbulence. Interestingly, for bubbles rising in grid-generated turbulence (or incident turbulence), Alm eras *et al.* (2017) determined a slightly larger value for b (≈ 0.7), where bubble-induced agitation appears to dominate. The mechanism was related to an increase in development length of the secondary bubble wake, which significantly enhances liquid velocity fluctuations. Indeed, the values of b from our DNS are smaller which is consistent with the notion that the background flow remains dominant for our parameter space considered.

7. Conclusions and outlook

In this study, we simulated the VC flow with dispersed light droplets between $Ra = 1.3 \times 10^8$ and 1.3×10^9 and Pr -value of 7. The liquid phase is simulated using DNS whereas the dispersed phase is simulated using an IBM with the interaction potential method for deformable interfaces. Our approach extends the IBM of Spandan *et al.* (2017) and Spandan *et al.* (2018a), where now the dispersed phase is fully coupled both mechanically and thermally to the flow. In addition, two datasets are simulated with and without thermal coupling to investigate its influence on the heat transport. Although Nu is slightly larger when the droplets are thermally coupled, we found that the VC flow with light droplets exhibits a non-monotonic change in heat transport with increasing Ra and largely retains the laminar-like VC scaling. We reason that a significant enhancement of heat transport depends crucially on a sufficiently strong droplet driving, which we show can be characterised by the relative strength of Ra_d to Ra and the bubble parameter, b .

When light droplets are introduced, the mean velocity and temperature profiles are highly skewed with the lowest Ra being most sensitive (figures 3 to 5). However, this sensitivity is masked by the Nu versus Ra trend, where we observe a non-monotonic behaviour with increasing Ra (figure 6a). This suggests the presence of competing mechanisms in the flow that contribute to the net heat transport. In contrast, the decreasing Re versus Ra trends are commensurate with the higher sensitivity at lower Ra , i.e. mechanical stirring is strongest at lowest Ra and higher α (figure 6b).

Based on analyses of the near-wall regions, we found that regions with higher values of local heat fluxes, Nu_{loc} , correspond to concomitant regions with higher values of skin-friction coefficient, $C_{f,loc}$, which is consistent with the notion that the local wind has influence over the local heat transport (figures 7 and 9). In turn, the strength of the local wind is related to whether the direction of the rising droplets aids or opposes the flow (figure 10). However, the trends of Nu_{loc} and $C_{f,loc}$ remain spatially non-monotonic and is sensitive to α . Based on these observations, we deduce that the results are specific to our selected simulation parameters and stress that the trends are non-universal.

The Nu versus Ra trend in figure 6 is different from recent experimental results by Gvozdić *et al.* (2018) for bubbly flow. Whilst Nu exhibits some Ra -dependency for our simulations with light droplets, Gvozdić *et al.* (2018) reported that Nu is largely insensitive to Ra for various volume fractions of droplets. The key distinction between our DNS and the experiments by Gvozdić *et al.* (2018) becomes readily apparent when we quantify the bubble parameter b and the droplet driving parameter Ra_d/Ra (cf. §6). Both b and Ra_d/Ra have a large separation in scales between the laboratory experiments and our DNS. More specifically, at $b \gtrsim O(10^{-1})$ and $Ra_d/Ra \gtrsim O(100)$, we anticipate that the dynamics of the dispersed phase-induced liquid agitations become overwhelmed by the dynamics of the background VC flow. For light droplets, both b and Ra_d/Ra are significantly lower. Therefore the local heat fluxes and skin friction coefficients exhibit non-universal behaviour, which reflects the dominance of the background VC flow.

Our results collectively indicate a non-universal heat transport behaviour for light droplets. Locally, the near-wall trends of heat fluxes and wall-shear stresses suggest the presence of competing mechanisms that, in concert, govern heat transport. One question that arises naturally here is: Can a universal trend be eventually obtained by increasing b and Ra_d/Ra for fixed Ra ? The answer to this question may provide some clues on disentangling the competing heat transport mechanisms in multiphase VC and is a subject for our future investigations.

Acknowledgements

We wish to express our gratitude to A. Prosperetti for the various fruitful discussions. This work is part of the research programme of the Foundation for Fundamental Research on Matter with project number 16DDS001, which is financially supported by the Netherlands Organisation for Scientific Research (NWO). The simulations were carried out on the national e-infrastructure of SURFsara, a subsidiary of SURF cooperation, the collaborative ICT organization for Dutch education and research. We also acknowledge PRACE for awarding us access to MareNostrum hosted by the Barcelona Supercomputing Center (BSC), Spain, under PRACE project number 2017174146.

Declaration of Interests

The authors report no conflict of interest.

REFERENCES

- AHLERS, G., GROSSMANN, S. & LOHSE, D. 2009 Heat transfer and large scale dynamics in turbulent Rayleigh–Bénard convection. *Rev. Mod. Phys.* **81**, 503–537.
- ALMÉRAS, E., MATHAI, V., LOHSE, D. & SUN, C. 2017 Experimental investigation of the turbulence induced by a bubble swarm rising within incident turbulence. *J. Fluid Mech.* **825**, 1091–1112.
- ARMFIELD, S. W. & PATTERSON, J. C. 1991 Direct simulation of wave interactions in unsteady natural convection in a cavity. *Int. J. Heat Mass Transfer* **34**, 929–940.
- BALACHANDAR, S. & EATON, J. K. 2010 Turbulent dispersed multiphase flow. *Annu. Rev. Fluid Mech.* **42**, 111–133.
- BRENNEN, C. E. 2005 *Fundamentals of Multiphase Flow*. Cambridge University Press.
- CHONG, K. L., LI, Y., NG, C. S., VERZICCO, R. & LOHSE, D. 2019 Convection-dominated dissolution for single and multiple droplets. *Submitted to J. Fluid. Mech.*
- CLIMENT, E. & MAGNAUDET, J. 1999 Large-scale simulations of bubble-induced convection in a liquid layer. *Phys. Rev. Lett.* **82**, 4827.
- DABIRI, S. & TRYGGVASON, G. 2015 Heat transfer in turbulent bubbly flow in vertical channels. *Chem. Eng. Sci.* **122**, 106–113.
- DECKWER, W.-D. 1980 On the mechanism of heat transfer in bubble column reactors. *Chem. Eng. Sci.* **35**, 1341–1346.
- DEEN, N. G. & KUIPERS, J. A. M. 2013 Direct numerical simulation of wall-to liquid heat transfer in dispersed gas–liquid two-phase flow using a volume of fluid approach. *Chem. Eng. Sci.* **102**, 268–282.
- DUINEVELD, P. C. 1995 The rise velocity and shape of bubbles in pure water at high Reynolds number. *J. Fluid Mech.* **292**, 325–332.
- GVOZDIĆ, B., ALMÉRAS, E., MATHAI, V., ZHU, X., VAN GILS, D. P. M., VERZICCO, R., HUISMAN, S. G., SUN, C. & LOHSE, D. 2018 Experimental investigation of heat transport in homogeneous bubbly flow. *J. Fluid Mech.* **845**, 226–244.
- GVOZDIĆ, B., DUNG, O.-Y., ALMÉRAS, E., VAN GILS, D. P. M., LOHSE, D., HUISMAN, S. G. & SUN, C. 2019 Experimental investigation of heat transport in inhomogeneous bubbly flow. *Chem. Eng. Sci.* **198**, 260–267.
- HUGHES, G. O. & GRIFFITHS, R. W. 2008 Horizontal convection. *Annu. Rev. Fluid Mech.* **40**, 185–208.
- JENNY, M., DUŠEK, J. & BOUCHET, G. 2004 Instabilities and transition of a sphere falling or ascending freely in a Newtonian fluid. *J. Fluid Mech.* **508**, 201–239.
- JOHNSON, T. A. & PATEL, V. C. 1999 Flow past a sphere up to a Reynolds number of 300. *J. Fluid Mech.* **378**, 19–70.
- KITAGAWA, A. & MURAI, Y. 2013 Natural convection heat transfer from a vertical heated plate in water with microbubble injection. *Chem. Eng. Sci.* **99**, 215–224.
- LAKKARAJU, R., SCHMIDT, L. E., ORESTA, P., TOSCHI, F., VERZICCO, R., LOHSE, D. &

- PROSPERETTI, A. 2011 Effect of vapor bubbles on velocity fluctuations and dissipation rates in bubbly Rayleigh–Bénard convection. *Phys. Rev. E* **84**, 036312.
- LANCE, M. & BATAILLE, J. 1991 Turbulence in the liquid phase of a uniform bubbly air–water flow. *J. Fluid Mech.* **222**, 95–118.
- LU, J., FERNÁNDEZ, A. & TRYGGVASON, G. 2005 The effect of bubbles on the wall drag in a turbulent channel flow. *Phys. Fluids* **17**, 095102.
- LUNDE, K. & PERKINS, R. J. 1998 *Shape oscillations of rising bubbles*. Springer.
- MATHAI, V., LOHSE, D. & SUN, C. 2020 Bubble and buoyant particle laden turbulent flows. *Annu. Rev. Condens. Matter Phys.* (In press.) .
- MERCADO, J. M., GOMEZ, D. C., VAN GILS, D. P. M., SUN, C. & LOHSE, D. 2010 On bubble clustering and energy spectra in pseudo-turbulence. *J. Fluid. Mech.* **650**, 287–306.
- MESCHINI, V., DE TULLIO, M. D., QUERZOLI, G. & VERZICCO, R. 2018 Flow structure in healthy and pathological left ventricles with natural and prosthetic mitral valves. *J. Fluid. Mech.* **834**, 271–307.
- MUDDE, R. F. 2005 Gravity-driven bubbly flows. *Annu. Rev. Fluid Mech.* **37**, 393–423.
- NG, C. S., OOI, A., LOHSE, D. & CHUNG, D. 2015 Vertical natural convection: application of the unifying theory of thermal convection. *J. Fluid Mech.* **764**, 349–361.
- NG, C. S., OOI, A., LOHSE, D. & CHUNG, D. 2017 Changes in the boundary-layer structure at the edge of the ultimate regime in vertical natural convection. *J. Fluid Mech.* **825**, 550–572.
- NG, C. S., OOI, A., LOHSE, D. & CHUNG, D. 2018 Bulk scaling in wall-bounded and homogeneous vertical natural convection. *J. Fluid Mech.* **841**, 825–850.
- ORESTA, P., VERZICCO, R., LOHSE, D. & PROSPERETTI, A. 2009 Heat transfer mechanisms in bubbly Rayleigh–Bénard convection. *Phys. Rev. E* **80**, 026304.
- PATTERSON, J. & IMBERGER, J. 1980 Unsteady natural convection in a rectangular cavity. *J. Fluid Mech.* **100**, 65–86.
- PIEDRA, S., LU, J., RAMOS, E. & TRYGGVASON, G. 2015 Numerical study of the flow and heat transfer of bubbly flows in inclined channels. *Int. J. Heat Fluid Flow* **56**, 43–50.
- VAN DER POEL, E. P., STEVENS, R. J. A. M. & LOHSE, D. 2011 Connecting flow structures and heat flux in turbulent Rayleigh–Bénard convection. *Phys. Rev. E* **84**, 045303.
- RENSEN, J., LUTHER, S. & LOHSE, D. 2005 The effect of bubbles on developed turbulence. *J. Fluid Mech.* **538**, 153–187.
- RISSO, F. 2018 Agitation, mixing, and transfers induced by bubbles. *Annu. Rev. Fluid Mech.* **50**, 25–48.
- SCHLICHTING, H. & GERSTEN, K. 2000 *Boundary-Layer Theory*, 8th edn. Springer.
- SCHWARZ, S., KEMPE, T. & FRÖHLICH, J. 2015 A temporal discretization scheme to compute the motion of light particles in viscous flows by an immersed boundary method. *J. Comput. Phys.* **281**, 591–613.
- SHISHKINA, O. 2016 Momentum and heat transport scalings in laminar vertical convection. *Phys. Rev. E* **93**, 051102.
- SHISHKINA, O., GROSSMANN, S. & LOHSE, D. 2016 Heat and momentum transport scalings in horizontal convection. *Geophys. Res. Lett.* .
- SHISHKINA, O., STEVENS, R. J. A. M., GROSSMANN, S. & LOHSE, D. 2010 Boundary layer structure in turbulent thermal convection and its consequences for the required numerical resolution. *New J. Phys.* **12**, 075022.
- SPANDAN, V., LOHSE, D., DE TULLIO, M. D. & VERZICCO, R. 2018a A fast moving least squares approximation with adaptive Lagrangian mesh refinement for large scale immersed boundary simulations. *J. Comput. Phys.* **375**, 228–239.
- SPANDAN, V., MESCHINI, V., OSTILLA-MÓNICO, R., LOHSE, D., QUERZOLI, G., DE TULLIO, M. D. & VERZICCO, R. 2017 A parallel interaction potential approach coupled with the immersed boundary method for fully resolved simulations of deformable interfaces and membranes. *J. Comput. Phys.* **348**, 567–590.
- SPANDAN, V., VERZICCO, R. & LOHSE, D. 2018b Physical mechanisms governing drag reduction in turbulent Taylor–Couette flow with finite-size deformable bubbles. *J. Fluid. Mech.* **849**.
- SUGIYAMA, K., CALZAVARINI, E. & LOHSE, D. 2008 Microbubbly drag reduction in Taylor–Couette flow in the wavy vortex regime. *J. Fluid Mech.* **608**, 21–41.
- DE TULLIO, M. D. & PASCAZIO, G. 2016 A moving-least-squares immersed boundary method

- for simulating the fluid–structure interaction of elastic bodies with arbitrary thickness. *J. Comput. Phys.* **325**, 201–225.
- UHLMANN, M. & CHOUippe, A. 2017 Clustering and preferential concentration of finite-size particles in forced homogeneous-isotropic turbulence. *J. Fluid Mech.* **812**, 991–1023.
- VERZICCO, R. & ORLANDI, P. 1996 A finite-difference scheme for three-dimensional incompressible flows in cylindrical coordinates. *J. Comput. Phys.* **123**, 402–414.
- VIOLA, F., MESCHINI, V. & VERZICCO, R. 2020 Fluid–Structure–Electrophysiology interaction (FSEI) in the left-heart: A multi-way coupled computational model. *Eur. J. of Mech.-B/Fluids* **79**, 212–232.
- WANG, S., VANELLA, M. & BALARAS, E. 2019 A hydrodynamic stress model for simulating turbulence/particle interactions with immersed boundary methods. *J. Comput. Phys.* **382**, 240–263.
- WANG, Y., SIERAKOWSKI, A. J. & PROSPERETTI, A. 2017 Fully-resolved simulation of particulate flows with particles–fluid heat transfer. *J. Comput. Phys.* **350**, 638–656.
- VAN WIJNGAARDEN, L. 1998 On pseudo turbulence. *Theor. Comput. Fluid Dyn.* **10**, 449–458.
- ZWIRNER, L. & SHISHKINA, O. 2018 Confined inclined thermal convection in low-Prandtl-number fluids. *J. Fluid Mech.* **850**, 984–1008.